Supporting Information

Liquid metal-assisted rapid joule heating for preparation of the Janus metal oxide in one second

Authors

Kaixuan Xi[a]#, Mengyang Cao[a]#, Sufang Li[a], Wenyu Yan[a], Guanqing Cheng[a], Yingpeng Wu[a], Lu Huang[a]**

[a] K. Xi, Dr. M. Cao, Prof. S. Li*, W. Yan, G. Cheng, Prof. Y. Wu, Prof. L. Huang*

State Key Laboratory of Chemo and Biosensing, College of Chemistry and Chemical Engineering, Advanced Catalytic Engineering Research Center of the Ministry of Education, Hunan University, Hunan Province, 410012, P. R. China.

#These authors contributed equally to this work

*Corresponding Author. E-mail: luhuang@hnu.edu.cn (L. Huang)

Note 1. Chemical Reagent

All metal oxides and solid metals (Al) used in this work were purchased from Shanghai Aladdin Biochemical Technology Co., Ltd., and were used as received without further purification. The liquid metal gallium was sourced from Beijing Jiya Semiconductor Materials Co., Ltd. (purity > 99.99%). The following chemical reagents were employed: potassium hydroxide (KOH, >95%, Shanghai Macklin Biochemical Co., Ltd.), ethanol (AR, Sinopharm Chemical Reagent Co., Ltd.), and Nafion membrane solution (Suzhou Zhengtaikang Scientific Research New Materials). Ultra-high purity argon gas and hydrogen-argon mixture gas were obtained from Changsha Saizhong Special Gases Co., Ltd. Ultrapure water was used throughout this work.

Note 2. Material Preparation

2.1 Synthesis of Janus-M

A precisely measured quantity of 200 mg of metal oxide material (e.g., Co_3O_4, Mn_3O_4, MnO_2) and 2 g of gallium (Ga) were placed into a 5 mL centrifuge tube. The mixture was vortex-mixed for 20 minutes to ensure complete encapsulation of the metal oxide particles by the gallium. Subsequently, the mixed material was transferred onto a carbon felt within a Joule heating setup. A carbothermal shock was applied for 1 seconds by passing an electrical current. The temperature of the shock was controlled by adjusting the power output of an external DC power supply, yielding products at different temperatures. The resulting product was then immersed in a 1 M aqueous KOH solution to recover the gallium. Finally, the remaining solid product was isolated by filtration, dried, and designated as J-M.

2.2 Controlled experiment - Slow heating comparison

Precisely weighed 500 mg of metal oxide material (e.g., Co_3O_4, Mn_3O_4, MnO_2) and 4 g of gallium (Ga) were placed into a 5 mL centrifuge tube. The mixture was vortex-mixed for 20 minutes to ensure complete encapsulation of the metal oxide particles by the gallium. The resulting mixture was then transferred into a crucible. The crucible was placed within a tube furnace, and the temperature was raised to 800°C at a heating rate of 5°C/min. After reaching 800°C, the sample was held at this temperature for 10

minutes. Subsequently, the sample was rapidly quenched using liquid nitrogen. The quenched product was then prepared for subsequent scanning electron microscopy (SEM) characterization.

2.3 Hydrothermal post-treatment

The synthesized J-MO material was combined with graphene oxide (GO) at different mass ratios. The mixture was dispersed in ethanol and subjected to hydrothermal treatment at 180 °C for 8 hours in a Teflon-lined autoclave. The resulting product was collected and freeze-dried for 24 hours. The freeze-dried material was then utilized for subsequent applications.

2.4. Controlled experiment - Solid metal

Precisely weighed 200 mg of metal oxide material (e.g., Co_3O_4, Mn_3O_4, MnO_2) and 2 g of solid metal powder were placed into an agate mortar and thoroughly ground for 10 minutes to achieve a homogeneous mixture. The resulting mixture was then transferred into a crucible. Subsequently, the mixture was placed onto a carbon felt within a Joule heating setup. A carbothermal shock was applied for durations ranging from 2 s to 3 min. The final products were collected.

2.5. The preparation process of wave-absorbing material

To integrate the Janus material with RGO, graphene oxide (GO) is mixed with the synthesized Janus material and subjected to hydrothermal treatment. The significant energy in the hydrothermal environment cleaves the oxygen-containing functional groups on the GO surface. Furthermore, reactive hydrogen radicals (H•) generated from the solvent attack the C-O bonds, progressively restoring the sp^2 carbon network and enhancing conductivity, thereby reducing GO to RGO[2].

Note 3. Materials Characterization

Sample characterization was performed using the following instrumentation: Morphology: Cold field-emission scanning electron microscopy (FESEM) was conducted using a Hitachi Regulus 8100 and a KYKY Technology EM8100 FESEM. High-Resolution Imaging: High-resolution transmission electron microscopy (HRTEM)

was performed on a JEOL JEM-F200 field-emission transmission electron microscope (JEOL Ltd., Japan). X-ray absorption fine structure (XAFS) Analysis: X-ray absorption fine structure (XAFS) spectroscopy was carried out using an easyXAFS300+ benchtop spectrometer. Crystallographic Analysis: X-ray diffraction (XRD) patterns were recorded on a Bruker D8 Advance diffractometer with Cu Kα radiation. Raman Spectroscopy: Raman spectra were acquired using an inVia Qontor confocal Raman microscope (Renishaw plc) equipped with 532 nm and 785 nm excitation lasers. Surface Chemistry: X-ray photoelectron spectroscopy (XPS) analysis was performed on a Thermo Scientific K-Alpha+ spectrometer. Magnetic Properties: Hysteresis loop measurements were conducted using a Lake Shore 8600 Series vibrating sample magnetometer (VSM). Electron Spin Resonance: Electron spin resonance (ESR) spectroscopy was performed using a JEOL JES-FA200 spectrometer (JEOL Ltd., Japan). Specific Surface Area: the BET test was conducted using the JW-BK200 surface area and pore size analyzer.

Note 4. Electromagnetic Wave Absorption Test

The coaxial line method is a classical approach for characterizing electromagnetic parameters (complex permittivity and permeability) of materials. In this study, a vector network analyzer (VNA, Ceyear 3672B) coupled with a coaxial air-line fixture (7 mm standard size) was employed for measurements. Prior to testing, the sample was precision-machined into a toroidal shape (outer diameter: 7.00±0.01 mm, inner diameter: 3.04±0.01 mm, thickness: 2.00±0.05 mm) to ensure optimal impedance matching with the fixture. After calibration (SOLT method) and background subtraction, the Nicolson-Ross-Weir (NRW) algorithm was applied to extract the complex permittivity ($\varepsilon = \varepsilon' - j\varepsilon''$) and permeability ($\mu = \mu' - j\mu''$) from the S-parameters. To validate reliability, the measurement error for polytetrafluoroethylene (PTFE) reference samples was controlled within ±5%.

The actual effective absorption bandwidth (EAB): This term refers to the frequency range where the reflection loss (RL) of the actual fabricated material sample measures below a specific threshold, for example -10 dB, in coaxial method measurements.

The simulated bandwidth: This term describes the frequency range over which the reflection loss (RL) falls below -10 dB. We obtain this result through electromagnetic

simulation software after artificially designing a specific multilayer structure based on the known intrinsic electromagnetic parameters of the material.

Note 5. Electrochemical Oxygen Evolution Test

Electrochemical measurements were performed using a Chi760e Instruments model CHI760e electrochemical workstation. A standard three-electrode configuration was employed: a glassy carbon working electrode (3 mm diameter), a platinum wire counter electrode (0.5 mm diameter x 37 mm length), and a saturated calomel reference electrode (SCE). Electrochemical experiments were conducted in a single-compartment electrochemical cell. The electrolyte was a 1 M aqueous potassium hydroxide (KOH) solution.

Catalyst ink preparation: Precisely 3 mg of the catalyst sample was weighed and transferred into a centrifuge tube. To this, 800 μL of ethanol, 150 μL of ultrapure water, and 50 μL of Nafion solution were added. The mixture was then ultrasonicated for 30 minutes to form a homogeneous dispersion.

Electrode preparation: The resulting catalyst ink was uniformly drop-cast onto the polished surface of the glassy carbon electrode (GCE) using a 10 μL micropipette. A total loading volume of 20 μL was applied. The modified electrode was subsequently dried at room temperature.

All measured potentials were converted to the reversible hydrogen electrode (RHE) scale using the following equation S1:

$$E_{RHE}=E_{SCE}+0.244\ V+0.0591\times pH \quad (S1)$$

Note 6. In-situ High-temperature EDS Testing

An external DC power supply was connected to the scanning electron microscope (SEM). A heating plate was affixed to the SEM sample stage using conductive carbon paste. The temperature of the heating plate was calibrated against the applied voltage; different temperatures were achieved by applying different voltages. An experiment was conducted at a calibrated temperature of 200 °C.

The cobalt oxide (Co_3O_4) powder was uniformly mixed with gallium, then cooled rapidly by liquid nitrogen, and subsequently cut in the middle for testing. After the temperature stabilized at 200 °C, samples of the Co_3O_4 powder were collected at 3-minute intervals. The collected samples were then transferred to the SEM stage for immediate analysis. The evolution of oxygen content in the Co_3O_4 particles was monitored over time using energy-dispersive X-ray spectroscopy (EDS) during the heating process.

Contrast experiment: After the cobalt oxide particles are delivered to the gallium surface, energy spectrum analysis tests will be conducted every 5 minutes on the unencapsulated cobalt oxide portion to observe the changes in oxygen content.

Note 7. In-situ High-temperature SEM Testing

The experimental setup is described above. Cobaltosic oxide (Co_3O_4) particles were encapsulated within liquid gallium (Ga). During heating, the dynamic morphological evolution of the gallium surface and the encapsulated Co_3O_4 particles was simultaneously recorded using a high-speed camera integrated with digital recording software.

Note 8. In-situ High-temperature XRD Testing

A homogeneous mixture of cobaltosic oxide (Co_3O_4) precursor and gallium (Ga) was prepared and loaded onto the high-temperature stage of an X-ray diffractometer. The chamber was evacuated and then backfilled with inert gas (e.g., argon) to a pressure of 0.3 MPa. The temperature was ramped at a rate of 30 °C/min. Diffraction patterns were collected in a step-scan mode (e.g., 0.02° 2θ step size) with a counting time of 0.1 minutes per degree 2θ. Data acquisition was performed at specific target temperatures: 25 °C, 100 °C, 200 °C, 300 °C, 400 °C, 500 °C, 600 °C, 700 °C, 800 °C, 900 °C, and 1000 °C. Upon reaching each target temperature, the sample was held isothermally for 10 minutes to ensure thermal equilibrium prior to data collection.

Note 9. Thermodynamic Calculation

The thermodynamic Gibbs free energy and enthalpy change were calculated by the HSC Chemistry software.

The equation inputs are shown in Note 10.

Note 10. Reaction equation

Carry out thermodynamic calculations and analysis using the following equation:

$$2Ga(l) + 3Co_3O_4 = Ga_2O_3 + 9CoO \quad (1)$$

$$2Ga(l) + 3Fe_3O_4 = Ga_2O_3 + 9FeO \quad (2)$$

$$2Ga(l) + 3Nb_2O_5 = Ga_2O_3 + 6NbO_2 \quad (3)$$

$$2Ga(l) + 3Mn_3O_4 = Ga_2O_3 + 9MnO \quad (4)$$

$$2Ga(l) + 6MnO_2 = Ga_2O_3 + 3Mn_2O_3 \quad (5)$$

Note 11. Finite Element Simulation Modeling

All finite element simulations in this work were performed using COMSOL Multiphysics® software.

Marangoni Flow Simulation: The Marangoni convection was modeled employing the Nonisothermal Flow interface coupled with the Marangoni Effect feature to account for surface tension gradients induced by temperature variations.

Heat Transfer Simulation in Liquid Metal Droplets: The heat transfer rates for liquid gallium (Ga) droplets of varying radii under Joule heating were simulated by solving a system of first-order partial differential equations (PDEs).

Multiphysics Simulation of Mass Transport: The mass transport of cobaltosic oxide (Co_3O_4) particles within liquid gallium under Joule heating was simulated using a multiphysics coupling approach. This model integrated the following physics interfaces: Laminar Flow (to model fluid dynamics of liquid Ga); Phase Field (to model the interface/tracking particle transport); General Form PDE (to model any additional custom physics, e.g., particle dynamics if not covered by other interfaces); Electric Currents (to model the Joule heating source); Heat Transfer in Solids (to model heat conduction).

Note 12. Life cycle-based cycle calculation.

We performed all calculations using Simapro 10.1 software and the Ecoinvent 3.10 database. The ReCiPe 2016 Midpoint (H) V1.08 / World (2010) H method provided the characterization factors for impact assessment. This environmental benefit analysis sets the system boundary as "from raw material entry to the core synthesis step of product formation," excluding raw material extraction, transportation, product use, and disposal. Standard dosages and units in all calculations adhere to the following standards: 1 kWh Electricity, high voltage [CN]; 1 Kg Co_3O_4 [GLO]; 1 Kg Gallium, semiconductor-grade [GLO].

In this experiment, energy consumption only considers the direct electricity input to the experimental apparatus (Joule heating device).

We calculated the "green index" for the experimental process using the following formula.

Calculation of gallium recovery rate: Calculate according to the following formula:

$$Recovery\ rate(n) = \frac{The\ dry\ weight\ recovered\ after\ the\ n\ use}{The\ dry\ weight\ recovered\ after\ the\ n-1\ use} \times 100\%$$

We weighed the weight of the gallium after its first use. We believe that after multiple uses, the recovery rate of gallium is approximately the same each time. The dry weight of recovered gallium after the first use is 1.92 g. The raw material of gallium is 2 g.

The calculation yields a gallium recovery rate of 96%.

Note 13. DFT calculations

All DFT calculations were performed using the Vienna Ab initio Simulation Package (VASP) employing the generalized gradient approximation (GGA) with the PBE functional. Plane waves describe valence electrons with an energy cutoff of 520 eV, whereas core electrons were represented by projector augmented-wave pseudopotentials (PAWs). For bulk and surface calculations, Monkhorst-Pack k-point grids of 12 × 12 × 12 and 5 × 5 × 1 were used. A lattice constant optimization was

performed on bulk Co_3O_4 and CoO. The Co_3O_4(111) and CoO(111) surface was generated by using a 2-layer 3 × 3 cell. A 15 Å vacuum was used to separate the slabs in the z-direction, and a dipole correction was applied. Each slabs were allowed to relax. All slabs and bulk were relaxed until all forces converged to less than 0.05 eV. The electronic energy convergence criterion was 10^{-6} eV. The formation can be defined as follows

$$E_{form} = E(Janus - Co) - E(Co_3O_4) - E(CoO)$$

Here, E(form) represents the formation energy of the Janus material. E(Janus-Co) denotes the lowest converged energy of the Janus material. E(Co_3O_4) corresponds to the lowest converged energy of the Co_3O_4 material. E(CoO) indicates the lowest converged energy of the CoO material.

Convert the "per supercell" energy into a more universal and comparable "per atom" energy, using the following formula:

$$\Delta E_f(meV/atom) = \frac{\Delta E_f(eV/supercell)}{N_{total\ atom}} \times 1000$$

Where, ΔE_f (eV/supercell) is the calculated formation energy of the entire supercell, which in this experiment is 1.26 eV. N_{total} atoms refers to the total number of atoms in the constructed supercell model. Here, N equals 48. Multiplying by 1000 converts the unit from eV to meV (1 eV = 1000 meV).

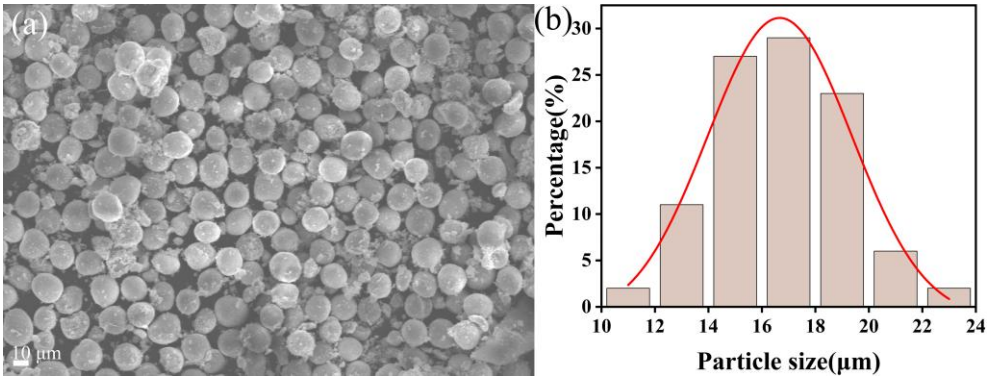

Figure S1. The overall morphology diagram of the Janus-Co. (a) SEM image of Janus-Co. (b) The particle size statistical distribution of the Janus-Co.

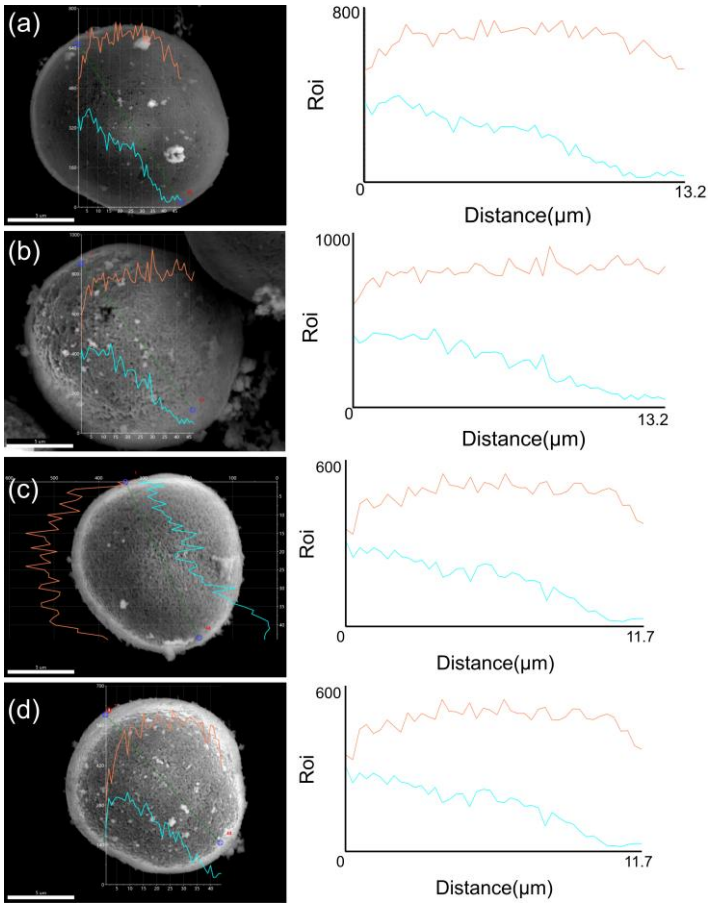

Figure S2. Perform EDS line scans on four different Janus-Co particles (a-d).

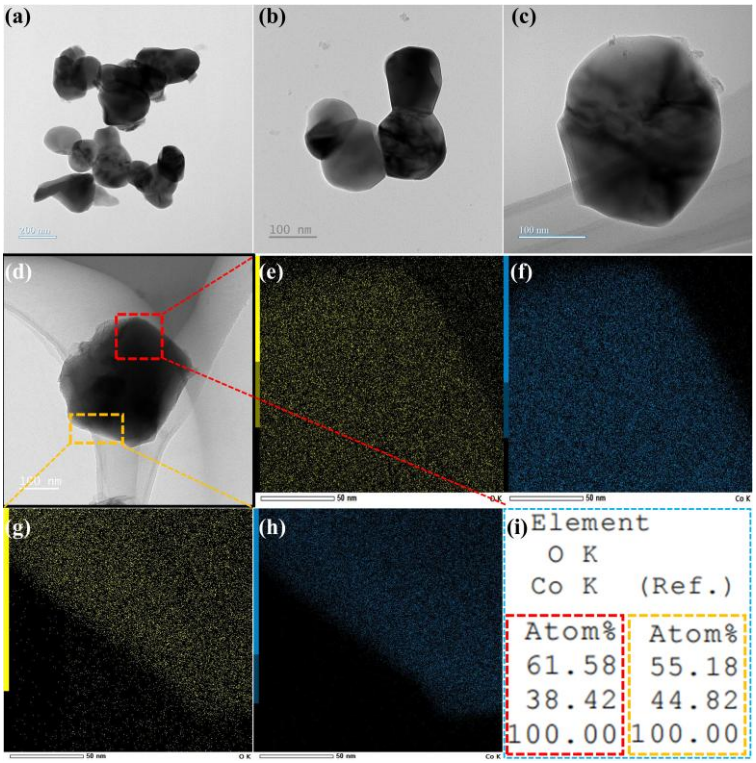

Figure S3. TEM spatial distribution characterization of the Janus-Co. (a-d) The morphological spatial distribution of the Janus-Co. (e-f) The EDS spatial distribution of O and Co in the upper half of the Janus-Co. (g-h) The EDS spatial distribution of O and Co in the lower half of the Janus-Co. (i) The red box and orange box show the atomic ratios of O atoms to Co atoms in the upper and lower halves of the Janus-Co.

Figure S3 clearly shows a distinct change in the atomic ratio between the upper and lower halves of the particle. This indicates the composite nature of the two materials. The upper half consists of Co_3O_4, with a ratio close to 4:3. The lower half is CoO, with a ratio approximately 1:1.

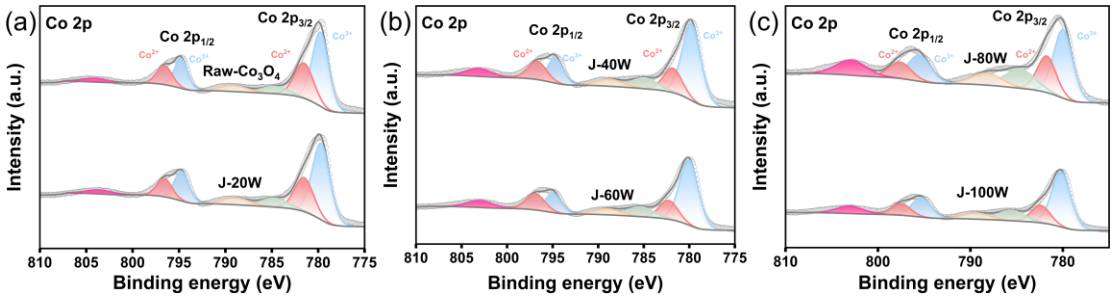

Figure S4. The Co 2P XPS spectra of the Janus-Co after processing with different powers. (a) Raw-Co_3O_4 and 20W. (b) 40 and 60W. (c) 80 and 100W.

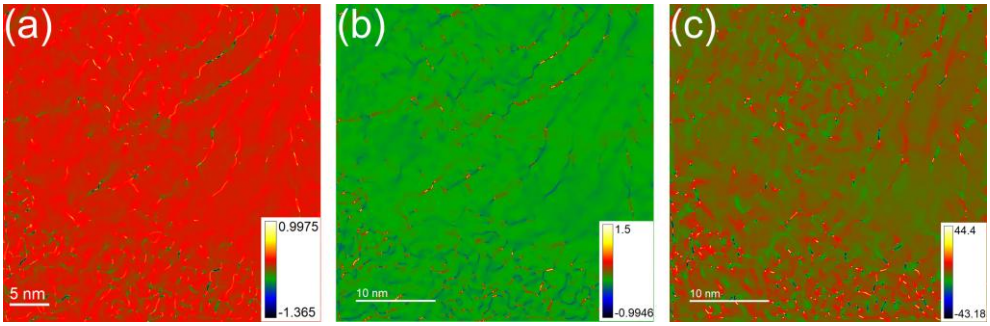

Figure S5. Perform geometric phase analysis (GPA) in different directions on high-resolution images. (a) e_{xy}. (b) d_{xy}. (c) r_{xy}.

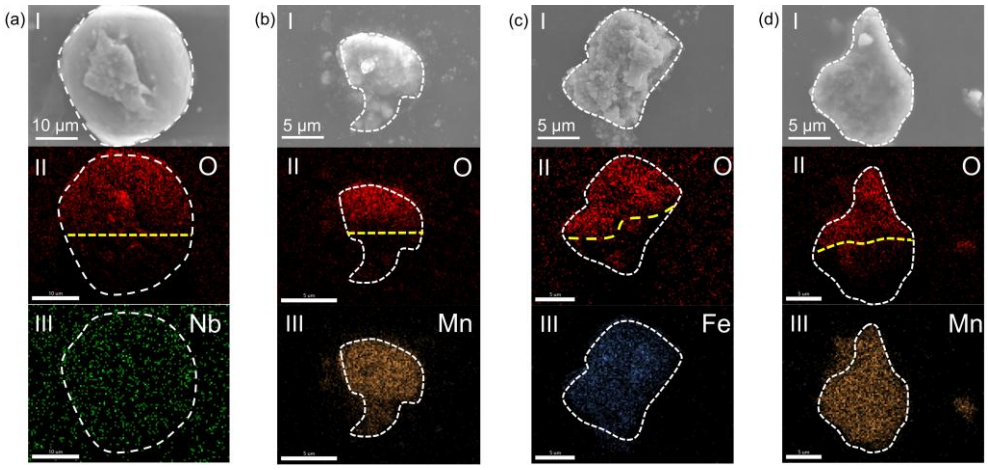

Figure S6. Product SEM and EDS characterization. (a) Nb_2O_5. (b) Mn_3O_4. (c) Fe_3O_4. (d) MnO_2.

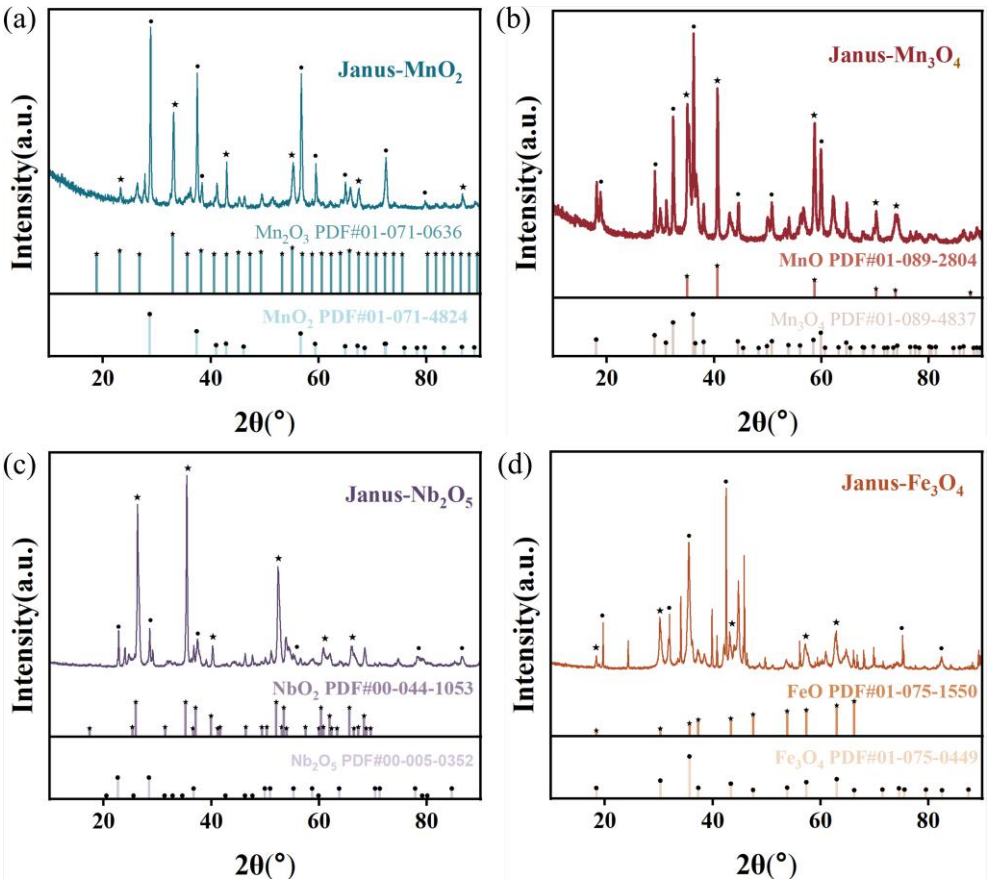

Figure S7. XRD characterization of different metal oxides after Joule heating treatment. (a) MnO_2. (b) Mn_3O_4. (c) Nb_2O_5. (d) Fe_3O_4.

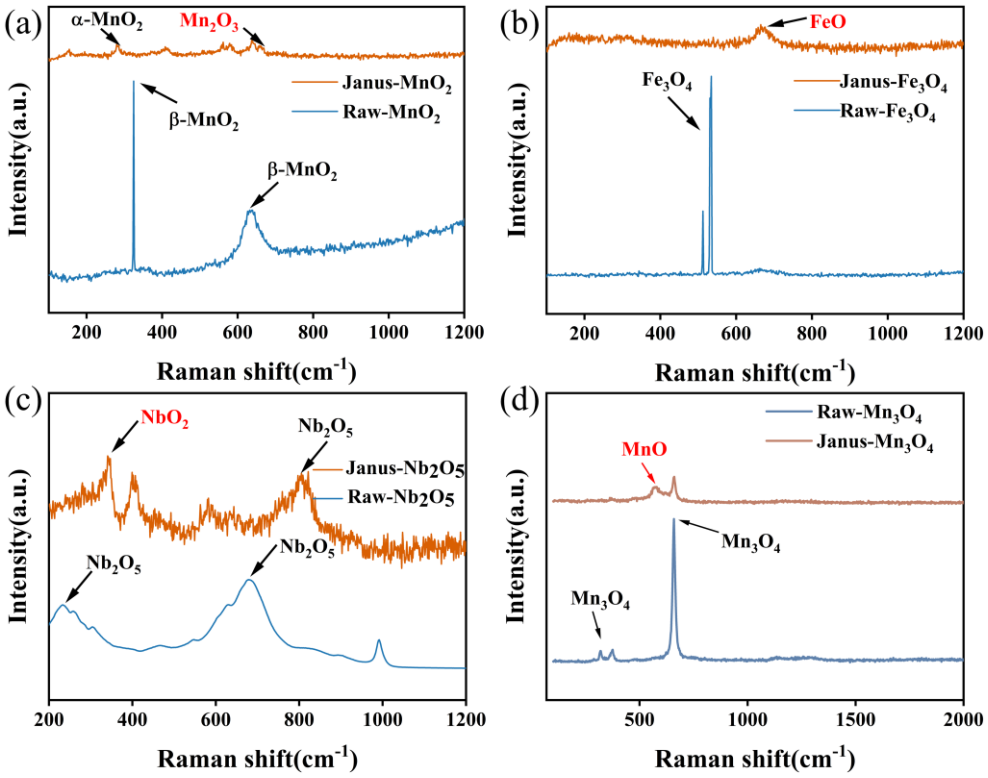

Figure S8. Raman characterization of different metal oxides after Joule heating treatment. (a) MnO_2. (b) Fe_3O_4. (c) Nb_2O_5. (d) Mn_3O_4.

Figure S9. The quality of Co_3O_4 Raw material.

Notes 14. To more definitively demonstrate the change in cobalt valence state, XPS analysis was performed on the products (Figure S4, S9-10). A clear shift of the binding energies towards lower values is observed with increasing temperature. Elevated temperature promotes the chemical reactions, and the strength of the lattice oxygen will gradually decrease, consistent with the partial reduction of Co_3O_4 to CoO.

The O 1s spectra (Figure S10) reveal a lower ratio of lattice oxygen to surface oxygen in the Joule-heated material compared to the starting material. This decrease aligns with the hypothesis of gallium's affinity for oxygen, indicating that oxygen is extracted from the metal oxide by gallium to form gallium oxide.

We performed peak fitting for cobalt and oxygen in various oxidation states, obtained their fitting areas, and plotted the trend of oxidation state changes with respect to temperature.

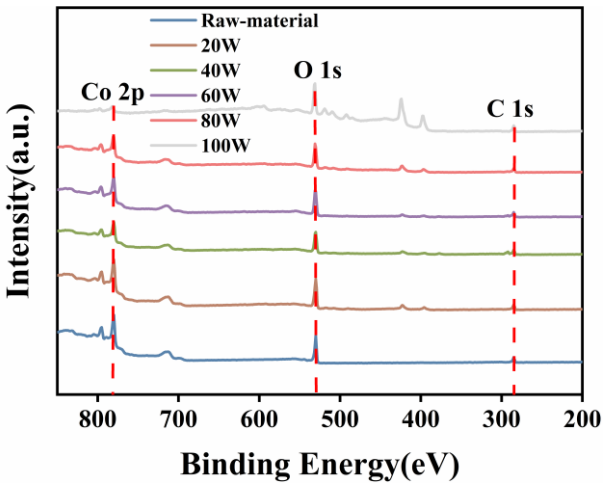

Figure S10. XPS spectrum of Janus-Co after treatment at different powers.

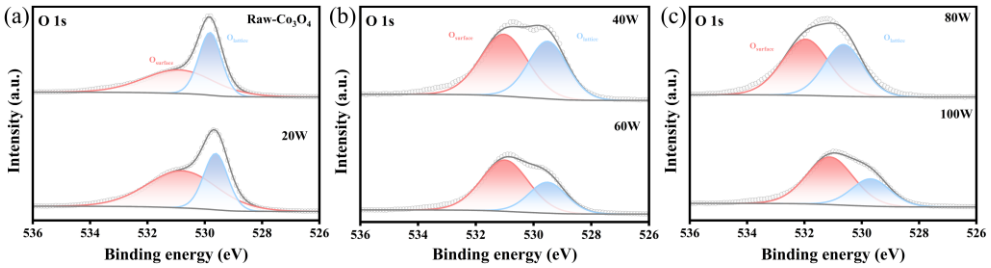

Figure S11. O 1s XPS spectral characterization of Janus-Co after treatment at different powers. (a) Raw-material and 20W. (b) 40W and 60W. (c) 80W and 100W.

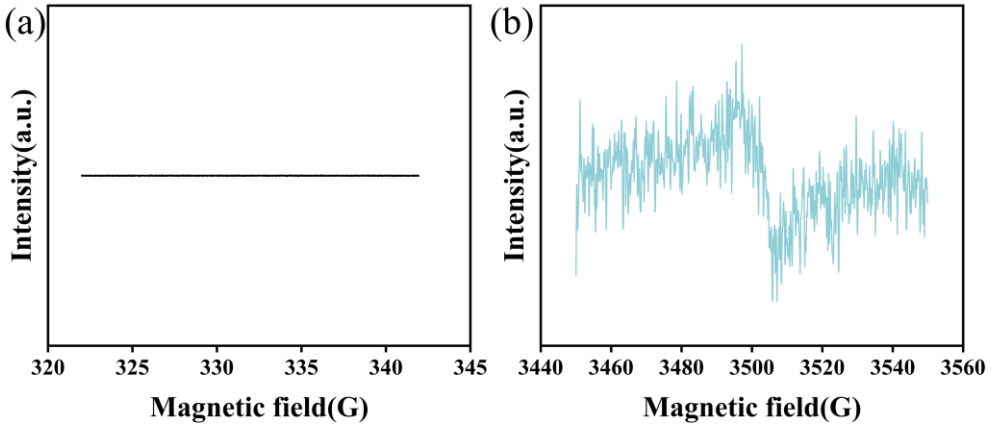

Figure S12. EPR characterization of the Janus-Co. (a) Raw-material. (b) Janus-Co fabricated via Joule heating treatment.

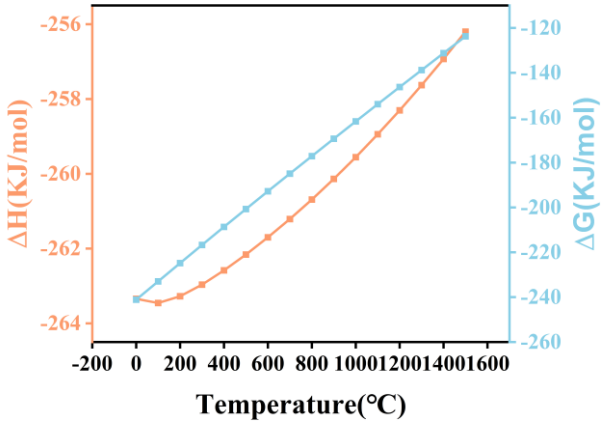

Figure S13. The Gibbs free energy and enthalpy change of the reaction of gallium with oxygen to form gallium oxide.

By calculation, it can be found that the reaction of gallium with oxygen to form gallium oxide is a spontaneous reaction, which fully proves that gallium has excellent affinity for oxygen. Concurrently, the reduction of metal cations (e.g., Co^{3+} + e- → Co^{2+}) by electrons donated from gallium weakens the M–O bonds, thereby promoting oxygen desorption. The liberated O^{2-} combine with gallium to form more thermodynamically stable Ga_2O_3 (Reaction: $4Ga + 3O_2 \rightarrow 2\ Ga_2O_3$, $\Delta G < 0$).

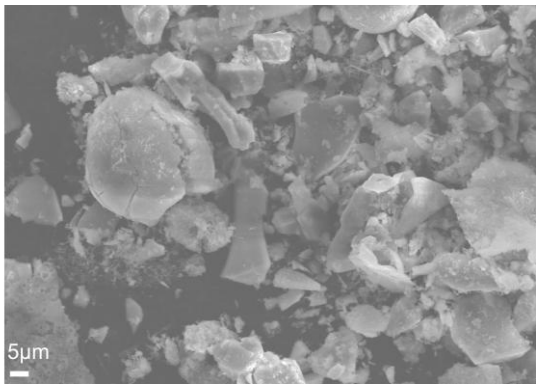

Figure S14. The mixture of Al powder and Co_3O_4, after undergoing Joule heating treatment, the resulting product. It can be seen that using other metals such as Al to replace Liquid metal Ga cannot serve as an oxygen-releasing agent.

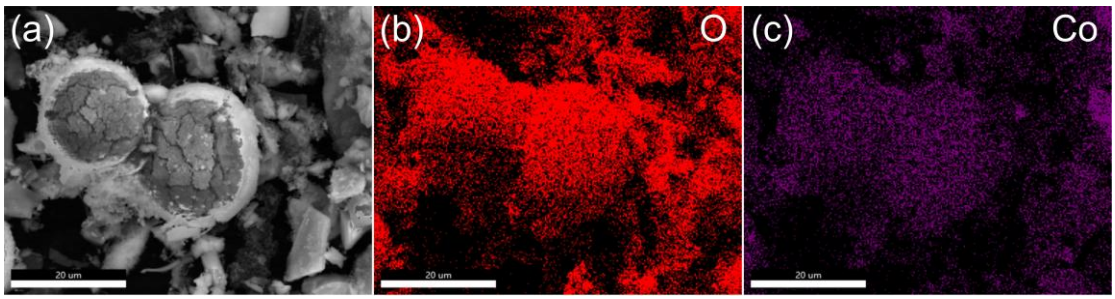

Figure S15. After a gradual temperature increase, the SEM characterization and EDS analysis of the product were conducted. (a) SEM image. (b) Distribution of oxygen element. (c) Distribution of cobalt element.

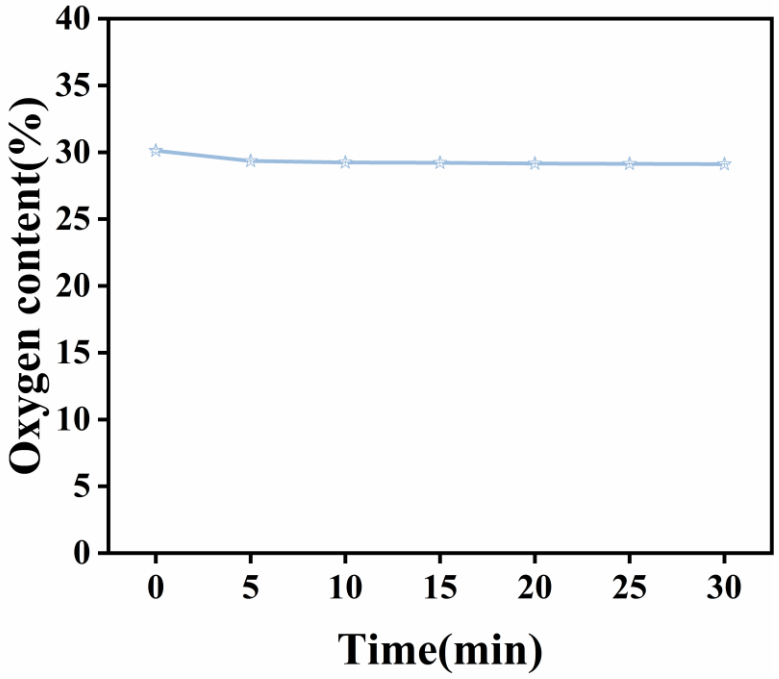

Figure S16. The change in oxygen content of Co_3O_4 particles on the Ga surface.

Semi-in-situ EDS testing for the Co_3O_4 particles that were exposed to the outer side of Ga was conducted. According to the oxygen content trend, it can be found that the oxygen content did not change significantly. This result should be caused by the following reason: the Co_3O_4 particles were transported to the surface of Ga through the Malagnini flow, avoided direct contact with Ga, and thus did not react with it.

Note 15. The EXAFS oscillation is caused by the interference between the backscattered wave and the emitted wave of the photoelectrons after they are scattered by the atoms around the absorbing atom. In this experiment, the jump height obtained under different reaction temperatures was different. Then, the experimental data are normalized using the following formula:

$$\chi(E) = \frac{\mu(E) - \mu_0(E)}{\mu_0(E_0)}$$

Here, E_0 represents the absorption edge, and μ_0(E) is the X-ray absorption of the atom. It is obtained through a low-order polynomial fitting based on the data before and after

the edge. By extrapolating both to the position of E_0, the jump height at the absorption edge is obtained, which is also $\mu_0(E_0)$.

The XAFS data c(E) in the energy space is transformed to the wave vector space c(k), with the aim of obtaining equal k intervals for subsequent Fourier transformation. The relationship is as follows:

$$k = \sqrt{2m_e(E - E_0)/h^2}$$

Here, m_e is the electron mass and h is the reduced Planck constant. In XAFS data acquisition, the signal attenuates strongly at high energies. After conversion to k-space, the high-k region exhibits significant decay. In practice, a weighting of k^n is often applied to compensate for this effect. The data used are thus $k^n c(k)$. In this experiment, we use n = 2.

The weighted k-space data c(k) is converted to obtain the radial distribution function, which is the R-space curve. Different peaks represent the coordination atoms at different positions.

In the wavelet transform spectrum, the vertical axis shows the coordination bond length R. The projection of the entire spectrum on the vertical axis is the same as that of the traditional Fourier transform curve. The horizontal axis shows the wave vector number k, which is the key to distinguishing different types of coordination atoms. Atoms with smaller atomic numbers have a weaker scattering ability for photoelectrons, and their strongest oscillation will appear in the low k region. In contrast, atoms with larger atomic numbers are the opposite, and their strongest oscillation will appear in the high k region.

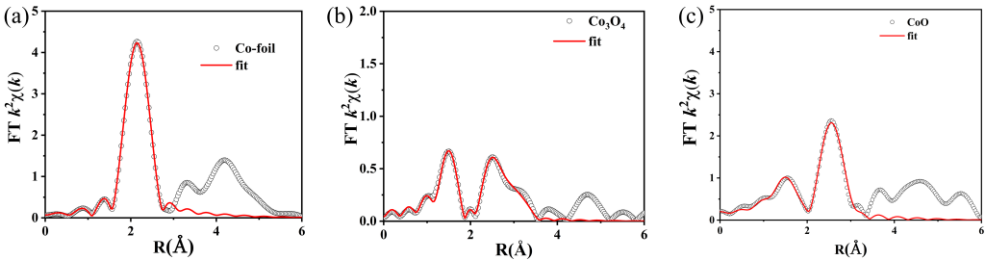

Figure S17. EXAFS spectra of the R-space curve of the Co *k*-edge fitting in the raw material. (a) Co-foil. (b) Co_3O_4. (c) CoO.

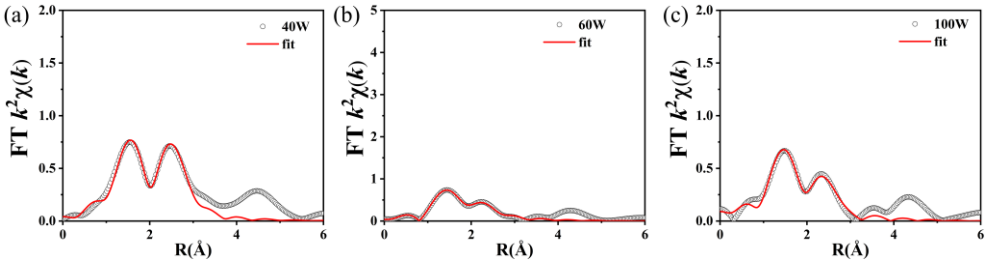

Figure S18. The extended edge fitting curves of the Janus-Co after processing with different powers - R-space curve curves. (a) 40W. (b) 60W. (c) 100W.

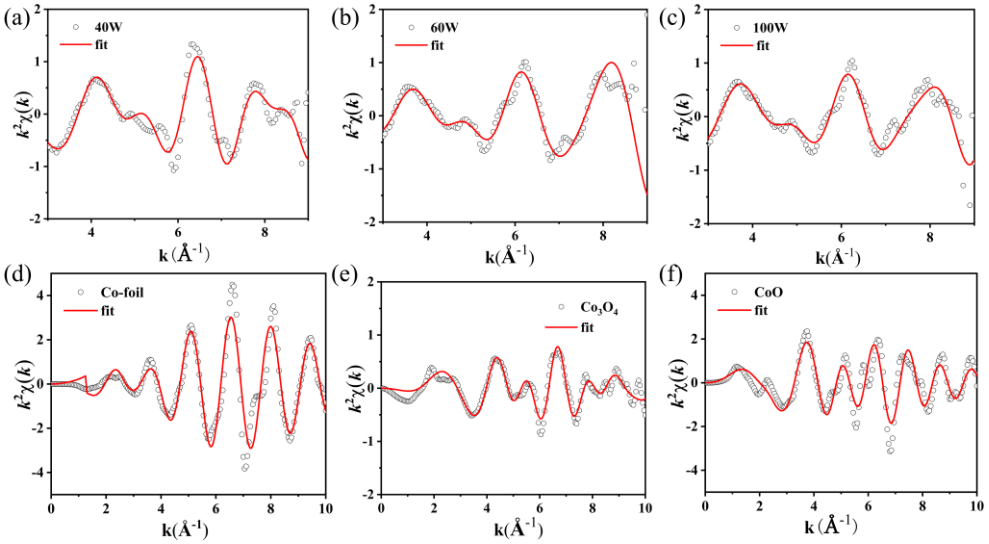

Figure S19. Co *K*-edge XAFS k^2 (χ(k)) oscillation curves. (a) 40W. (b) 60W. (c) 100W. (d) Co-foil. (e) Co_3O_4. (f) CoO.

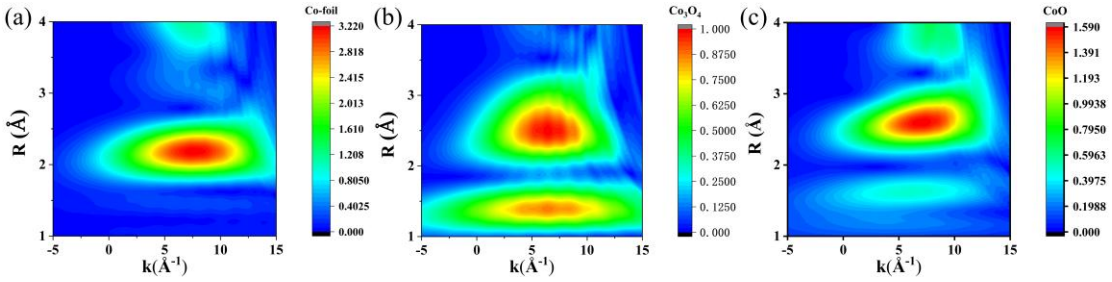

Figure S20. Analysis of raw material wavelet transform. (a) Co-foil. (b) Co_3O_4. (c) CoO.

Note 16. The surface tension of gallium can be calculated using the equation S2 as follows. It can be seen that the surface tension of gallium decreases as the temperature rises[1].

$$\gamma = 708 - 0.066 \times (T - 29.8) \quad \text{(S2)}$$

Where γ is surface tension, T is centigrade degree.

The finite element method was used to simulate the heating rate of gallium under the action of Joule heating at different radii. It was found that the heating rate was extremely fast, which is consistent with our experimental results. That is, the heating rate under Joule heating is very fast, providing a theoretical possibility for the subsequent generation of Marangoni flow.

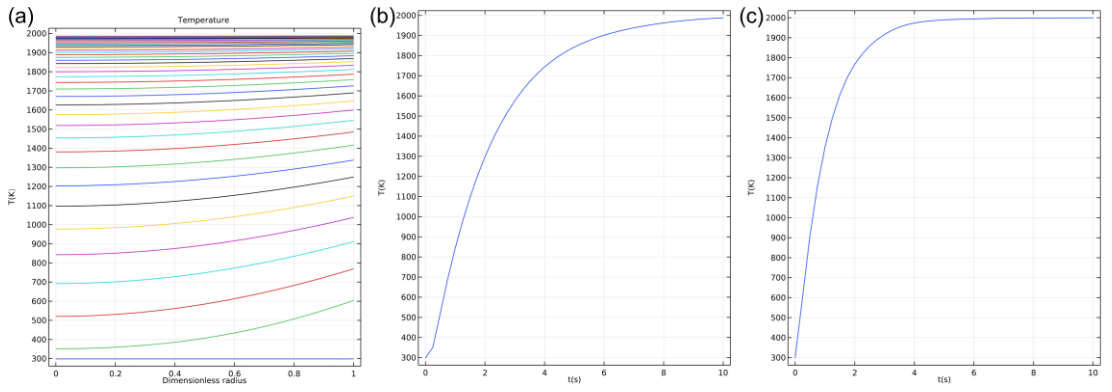

Figure S21. The finite element method was used to simulate the heating rate of gallium at different radii under the effect of Joule heating. (a) Simulate the temperature curves for all radii. (b) Radius is 2.5 mm. (c) Radius is 5 mm.

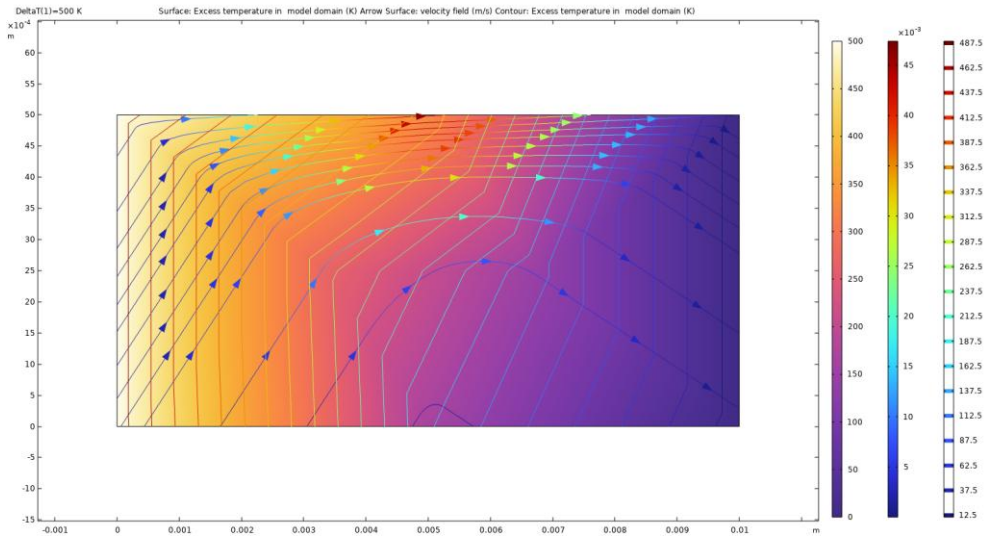

Figure S22. The Marangoni flow phenomenon when the temperature difference is 500 K.

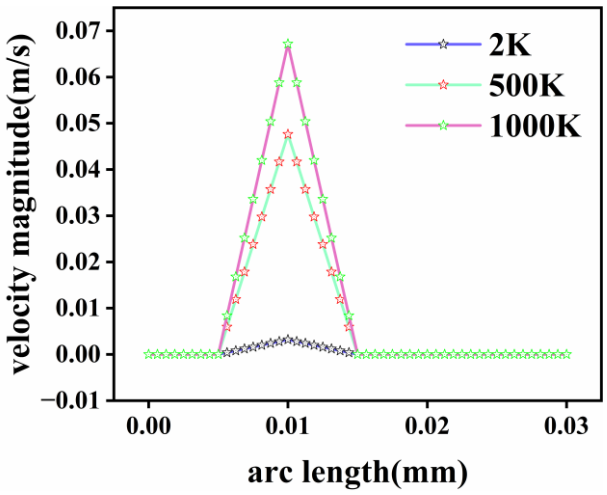

Figure S23. When the temperature difference is 2K, 500K and 1000K, the difference in their velocity magnitudes. The mass transfer rate of substances within the gallium phase under different temperature differences was analyzed. It was found that as the temperature difference increased, the transfer rate also increased, which was consistent with our experimental results.

Note 17. We simulated the situation under the effect of Joule heating, both when the reaction did not occur and one second after it occurred. It was found that one second after the reaction occurred, significant changes occurred in the velocity vector of cobalt

trioxide and the distribution of the pressure field compared to the situation when the reaction did not take place. This proves that due to the existence of the Marangoni flow, the metal oxides change their distribution state in an extremely short period of time and then undergo the subsequent oxygen-reduction reaction.

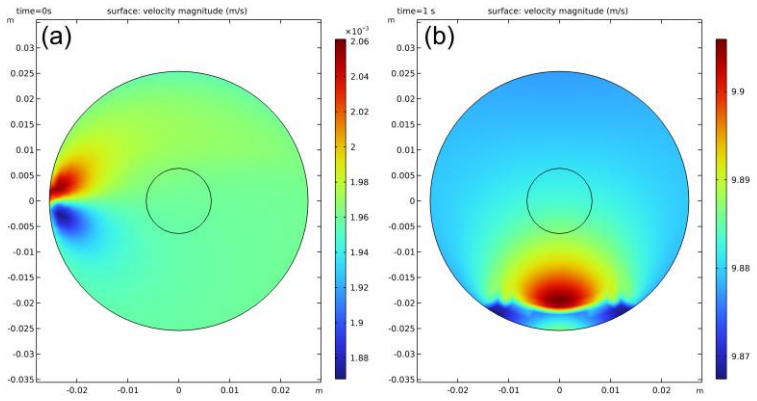

Figure S24. The distribution of velocity magnitude at different times. (a) Time=0 s. (b) Time=1 s.

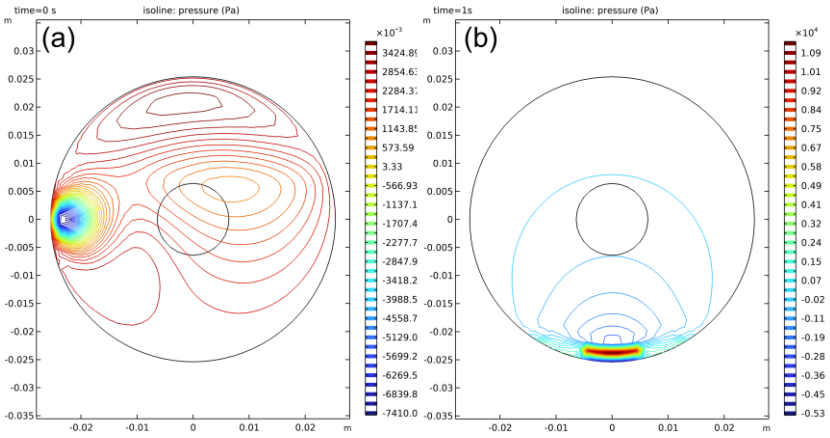

Figure S25. The distribution of pressure fields at different times. (a) Time=0 s. (b) Time=1 s.

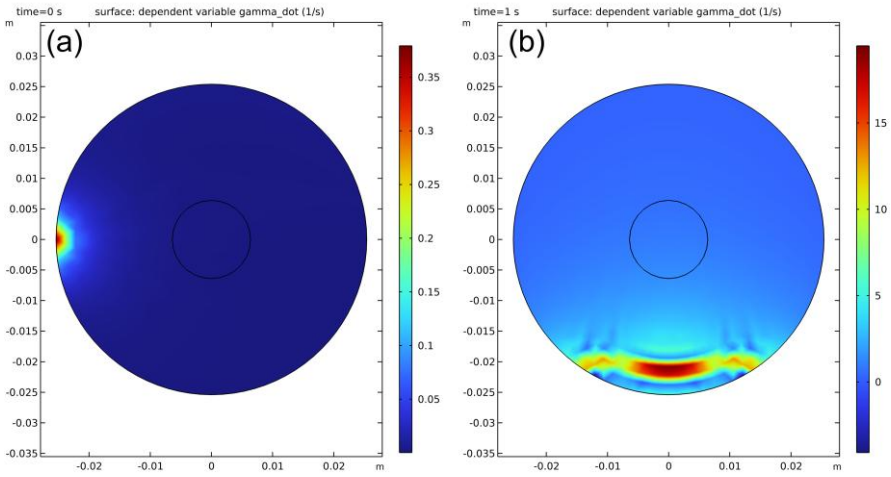

Figure S26. The distribution of dependent variable gamma at different times. (a) Time=0 s. (b) Time=1 s.

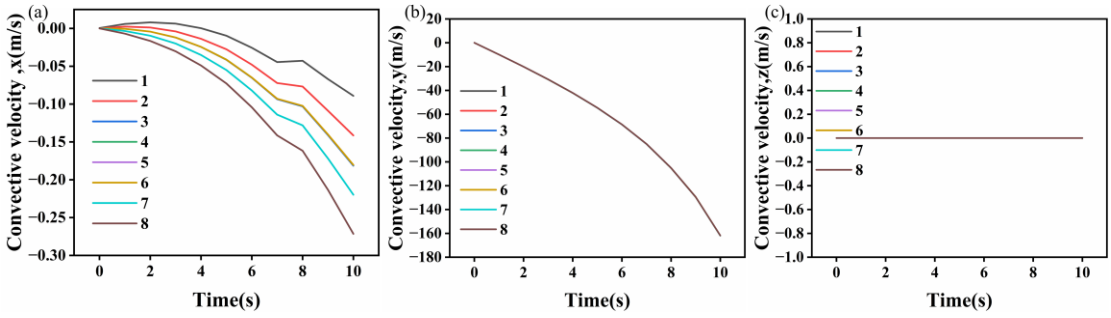

Figure S27. The convective velocities of Co_3O_4 in different directions within gallium. (a) x direction. (b) y direction. (c) z direction.

Note 18. We subjected the product obtained from Joule heating treatment of a mixture of Co_3O_4 and gallium (Ga) to instantaneous quenching in liquid nitrogen. Subsequently, the quenched sample was sectioned through its center. Furthermore, examination of the Ga surface indicated that only a portion of the Co_3O_4 particles present were effectively wetted/infiltrated by the Ga. This observed heterogeneity is consistent with the presence of Marangoni flow during the process. This flow rapidly transported Co_3O_4 particles to the Ga surface within an extremely short timeframe. Consequently, Ga rapidly extracted oxygen from only a subset of these particles upon their arrival at the surface. This differential deoxygenation resulted in an oxygen-asymmetric distribution across the particle population, ultimately leading to the formation of a Janus structure.

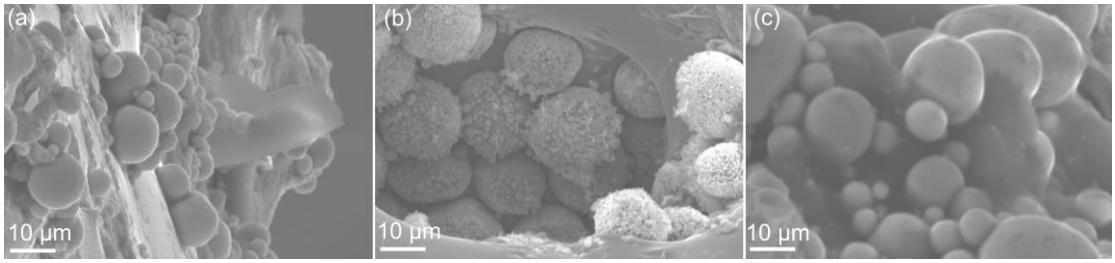

Figure S28. The cross-sectional SEM image of the product obtained after the sample was subjected to Joule heating treatment and then rapidly cooled with liquid nitrogen. The distribution of Co_3O_4 in the cross-section of gallium(a-b) and gallium surface(c).

Note 19. Based on the theory of electromagnetic wave reflection at dielectric interfaces and the law of energy conservation, the following formula (1-5) is derived through the reflection coefficient and impedance matching relationships.

$$RL(dB) = 20\log_{10}\frac{|Z_{in}-Z_0|}{|Z_{in}-Z_0|} \quad (1)$$

$$Z_{in} = \sqrt{\frac{\mu_0}{\varepsilon_0}}\sqrt{\frac{\mu_r}{\varepsilon_r}}tanh(j2\pi fd\sqrt{\mu_r\varepsilon_r}/c) \quad (2)$$

$$Z_0 = \sqrt{\frac{\mu_0}{\varepsilon_0}} \quad (3)$$

$$Tan\delta_\varepsilon = \varepsilon''/\varepsilon' \quad (4)$$

$$Tan\delta_\mu = \mu''/\mu' \quad (5)$$

Where Z_{in} is the input impedance, Z_0 is the impedance of free space (approximately 370 Ω), *c* is the speed of light, f is the electromagnetic wave frequency, d is the thickness of the absorber material, and μ_r and ε_r are the complex permeability and complex permittivity of the absorber material, respectively. The ratio of the components was first optimized (Figure S29-31). It was found that at a raw material to RGO ratio of 1:3 and an absorber thickness of 2 mm, the reflection loss reached approximately -30 dB, with a maximum effective absorption bandwidth (EAB) of about 4 GHz. When the ratio was either lower or higher than 1:3, the reflection loss decreased.

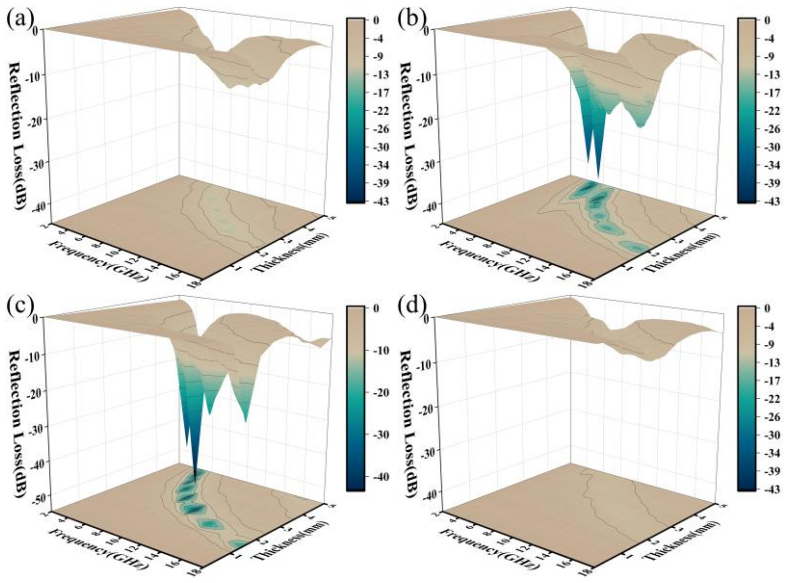

Figure S29. Three-dimensional absorption performance diagrams of the Janus-Co mixed with GO at different proportions. (a) 1:1. (b) 2:1. (c) 3:1. (d) 4:1.

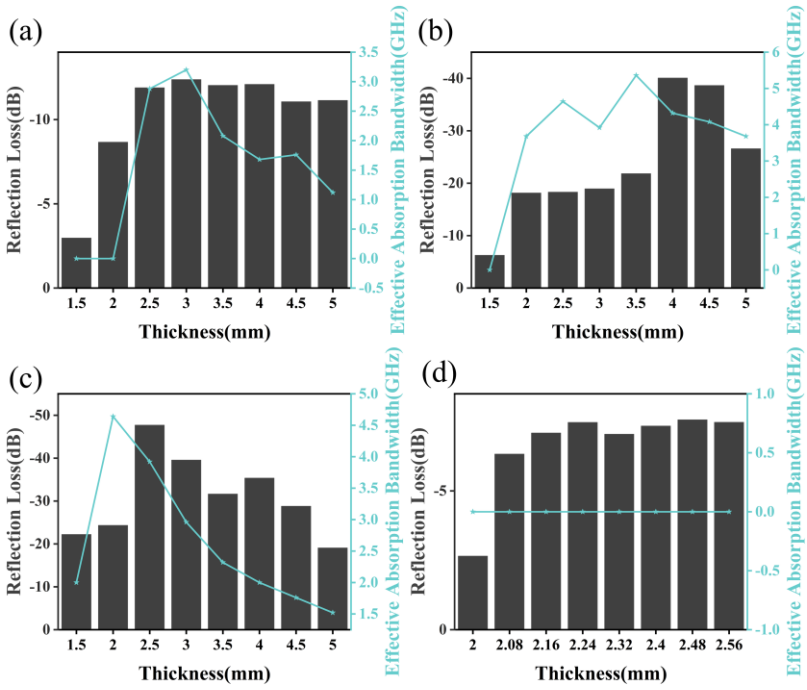

Figure S30. EAB of Janus-Co/GO blends with different mixing ratios (coaxial-line method). (a) 1:1. (b) 2:1. (c) 3:1. (d) 4:1.

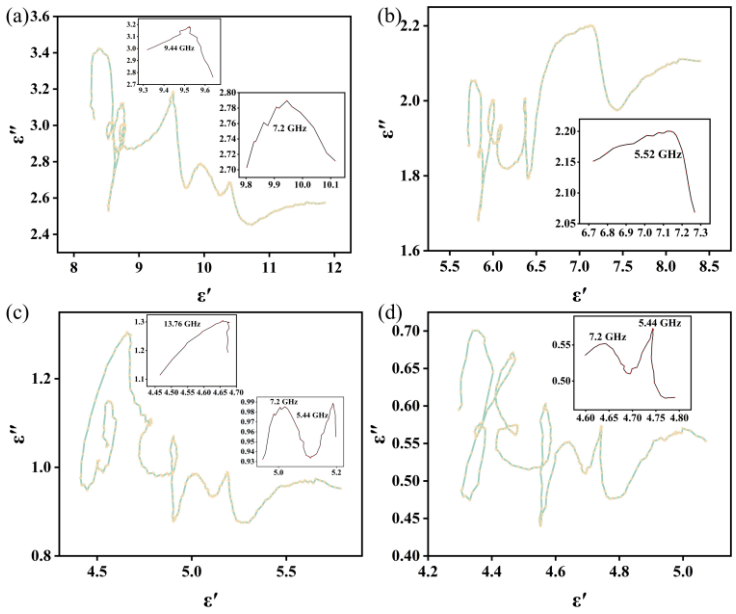

Figure S31. Cole-Cole plots of the mixture of Janus-Co and GO with different proportions. (a) 1:1. (b) 2:1. (c) 3:1. (d) 4:1.

$$\varepsilon''(\omega) = \varepsilon_p'' + \varepsilon_c'' = (\varepsilon_S - \varepsilon_\infty)\frac{\omega\tau}{1+\omega^2\tau^2} + \frac{\sigma}{\varepsilon_0\omega} \quad \text{(S3)}$$

where σ, ω are the electrical conductivity and angular frequency, respectively.

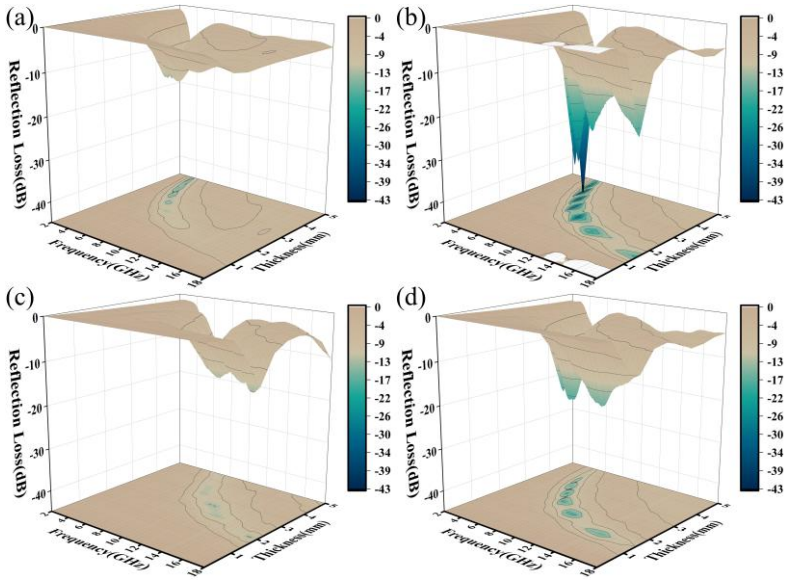

Figure S32. The three-dimensional absorbing properties of the Janus-Co under different power levels. (a) 20W. (b) 40W. (c) 60W. (d) 80W.

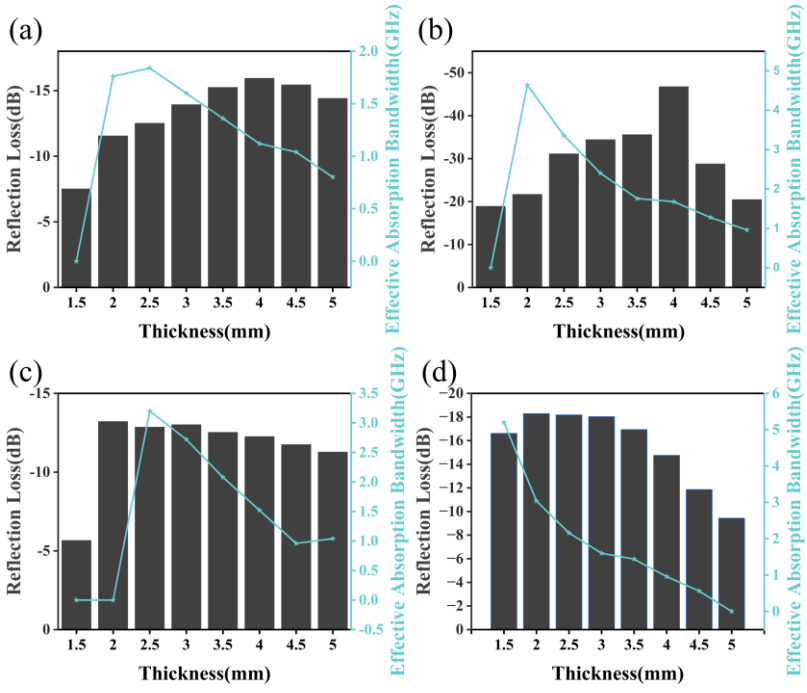

Figure S33. EAB of Janus-Co under different power levels (coaxial-line method). (a) 20W. (b) 40W. (c) 60W. (d) 80W.

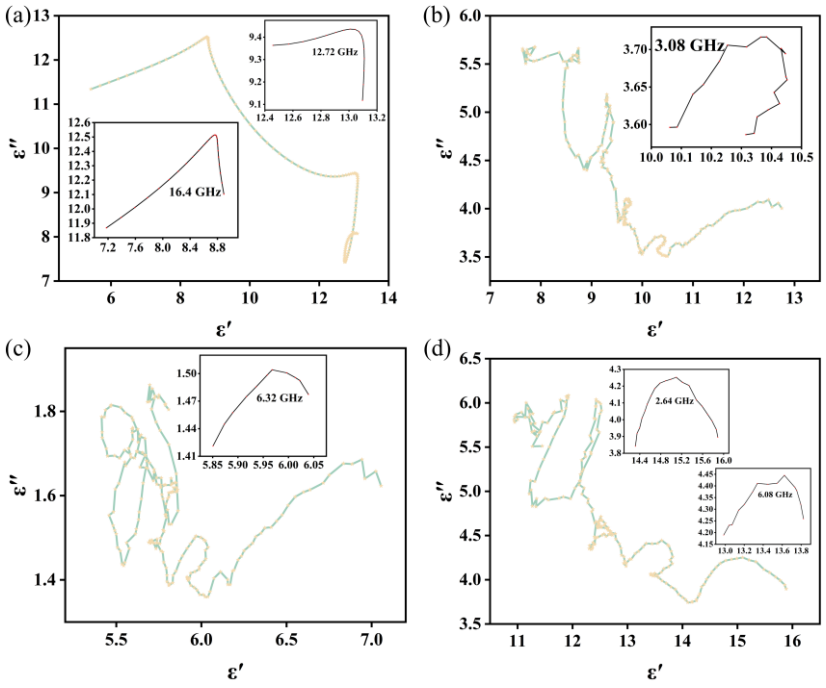

Figure S34. Cole-Cole plots of the Janus-Co under different power levels. (a) 20W. (b) 40W. (c) 60W. (d) 80W.

Note 20. RCS and its field analysis simulation steps.

The monostatic radar cross section (RCS) results of the materials were simulated using the CST STUDIO SUITE 2022 software. Firstly, input the permittivity and permeability of the experiment into the simulation software and set the solution type to the time-domain solver. Then, the perfect conducting electrode (PEC) (300 × 300 × 0.5 mm) and an absorber layer (300 × 300 × d = RL_{min} mm) are modeled. Finally, the simulation yields the result.

In addition, the CST STUDIO SUITE 2022 software is used to simulate the periodic structures to calculate the electric field distribution (E-filed), magnetic field distribution (H-filed) and power loss distribution. The dielectric constant and magnetic permeability of the experiment were input into the simulation software. Set periodic boundaries and use a frequency-domain solver. The simulation frequency in simulation conditions was

set as 3.5608, 9.312, and 13.17 GHz, respectively. The gradient structure of this design is composed of three cubes. The size of the bottom layer model is 10 × 10 × 4 mm, the size of the middle layer model is 8 × 8 × 2 mm, and the size of the upper layer model is 6 × 6 × 4 mm.

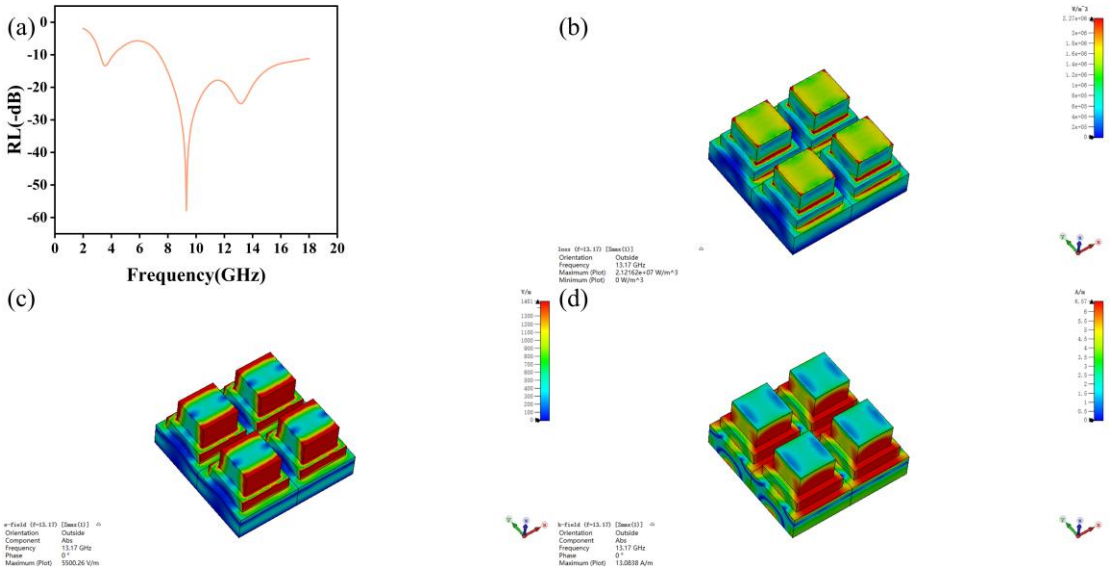

Figure S35. The simulation results of the composite gradient structure. (a) Simulation reflection loss-frequency curve. (b) Power loss at a frequency of 13.17 GHz. (c) Electrical field loss at a frequency of 13.17 GHz. (d) Magnetically induced losses at a frequency of 13.17 GHz.

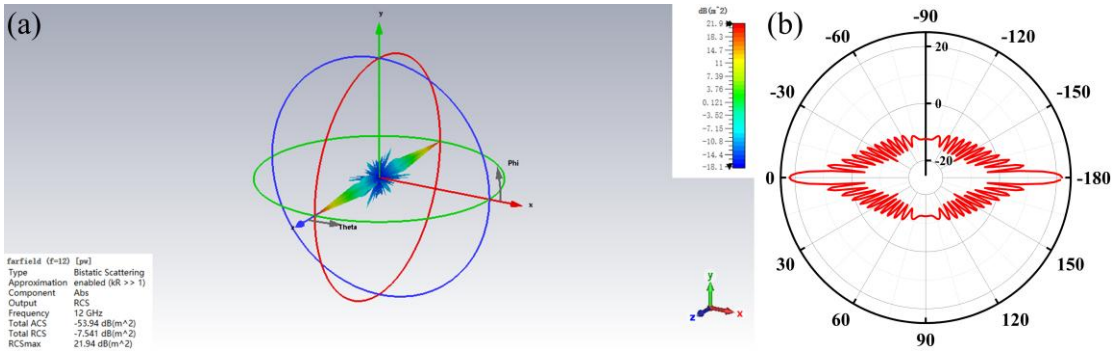

Figure S36. The three-dimensional radar wave scattering signal and the RCS in the polar coordinate system of the PEC plate.

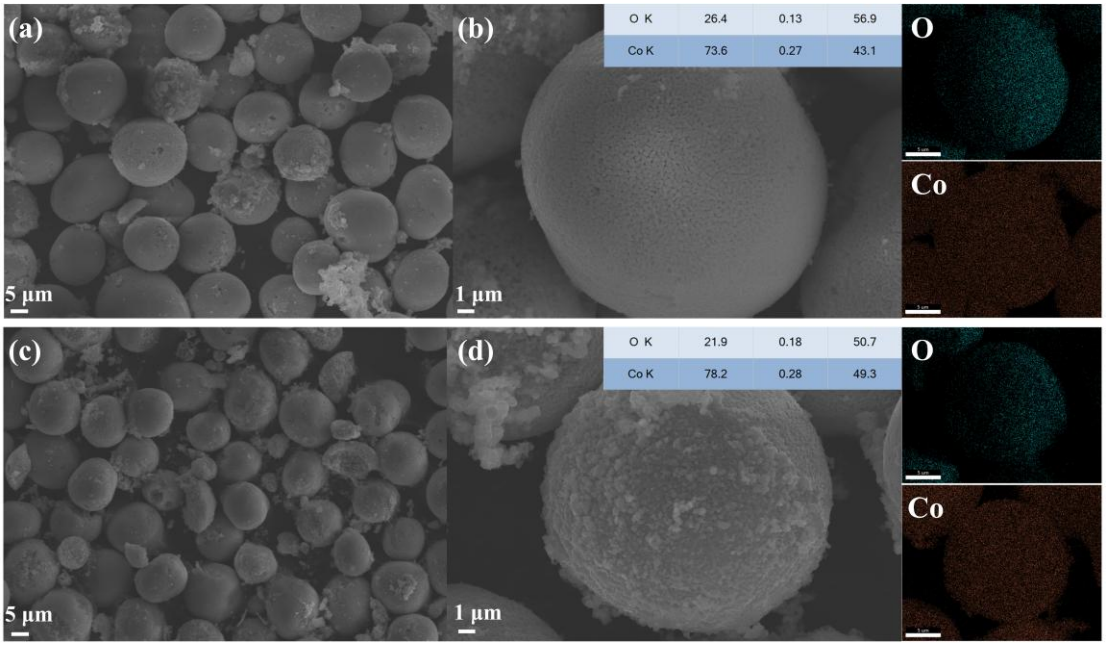

Figure S37. Comparison of SEM and EDS Characterizations of Samples Before and After Long-Term Stability Cycling Test. (a-b) Before long-term stability cycling test; (c-d) After long-term stability cycling test.

Note 21. We measured the temperature of heated carbon felt by placing a temperature probe against its surface, connected to a temperature display. Different levels of electrical power were applied to the carbon felt using a DC power supply, and the corresponding temperatures were recorded. The relationship between temperature and applied power was then derived by fitting the data (Equation S4). All experiments were performed in triplicate.

$$y = 12.96x + 106.09 \quad \text{(S4)}$$

Where y is temperature, x is power.

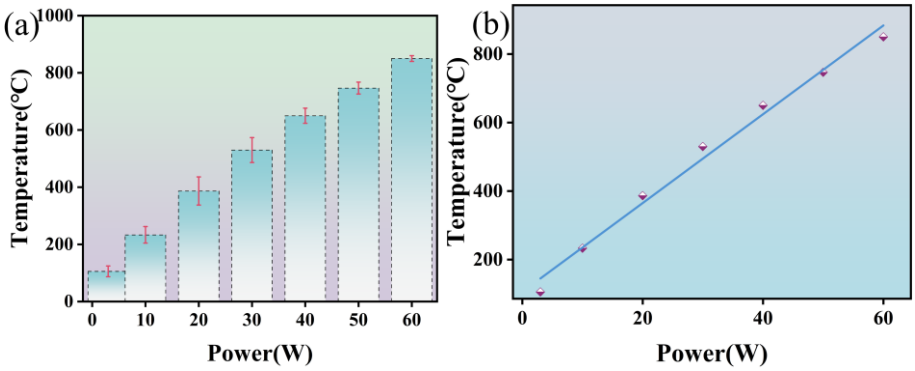

Figure S38. Power and Temperature Relationship Graph. (a) The relationship between power and temperature obtained from three parallel experiments. (b) The fitting curve of temperature and power.

Table S1. Quantitative Indicators in “Green Chemistry”.

	Yield	Gallium recovery rate
Number	~90%	96%

Table S2. EXAFS fitting parameters at the Co K-edge for various samples (S_0^2=0.71).

Samples	shell	CN[a]	R[b](Å)	σ^{2c}(Å^2)	ΔE_0[d](eV)	R factor
Co-foil	Co-Co	12*	2.48±0.01	0.0062	6.3±0.5	0.0018
CoO	Co-O	6*	2.09±0.04	0.0137	2.9±1.0	0.006
	Co-Co	12*	3.00±0.02	0.0102		
Co_3O_4	Co-O	4*	1.99±0.04	0.0056	7.9±1.9	0.017
	Co-Co	12*	3.47±0.01	0.0069		
J-60	Co-O	6.17±0.9	2.06±0.07	0.0071	-2.1±0.3	0.007
	Co-Co	6.05±0.9	3.22±0.10	0.0061		
J-40	Co-O	6.10±0.8	1.96±0.01	0.0049	-8.8±0.2	0.008
	Co-Co	4.27±0.9	2.99±0.03	0.0036		
J-100	Co-O	5.34±0.7	2.03±0.09	0.0055	-4.3±0.7	0.006
	Co-Co	4.11±0.9	3.03±0.01	0.0083		

[a]*CN*: coordination numbers; [b]*R*: bond distance; [c]σ^2: Debye-Waller factors; [d] ΔE_0: the inner potential correction. R factor: goodness of fit. Error bounds that characterize the structural parameters obtained by EXAFS spectroscopy were estimated as CN±20%; R ± 1%; σ^2 ± 20%.

Table S3. Comparison of formation energy of different systems.

material system	ΔE_f(eV/supercell)	References
Janus Co_3O_4/CoO	1.26	This work
MoS_2-$(C_4H_9NH_3)_2(CH_3NH_3)_3Pb_4I_{13}$	2	Ref.3
graphene/WS_2	2.26	Ref.4
graphene/MoS_2	2.08	Ref.4
graphene/graphene	1.37	Ref.4

Reference:

[1] S. Hardy, *Journal of Crystal Growth.* **1985**, 71, 602.

[2] X. Xiang, Y. Zhu, C. Q. Gao, H. Du, C. W. Guo, *Carbon Lett.* **2022**, 32, 557.

[3] M. Moazzami Gudarzi, S. H. Aboutalebi, Mapping the Binding Energy of Layered Crystals to Macroscopic Observables. *Adv. Sci.* 2022, 9, 2204001. **https://doi.org/10.1002/advs.202204001**.

[4] Changcheng Xu, Yong Ding, Shaofeng Wang, Shuo Cao. The van der Waals interaction and absorption and electron circular dichroism spectra of two-dimensional bilayer stacked structures. *Spectrochimica Acta Part A: Molecular and Biomolecular Spectroscopy,* 2023, 303(123182), 1386-1425. https://doi.org/10.1016/j.saa.2023.123182.